

# Raman Characterization of the Charge Density Wave Phase of 1T-TiSe<sub>2</sub>: From Bulk to Atomically Thin Layers

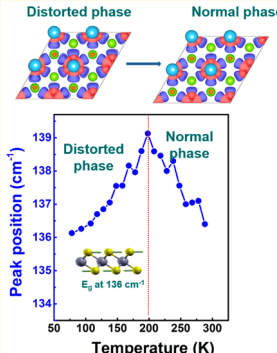
Dinh Loc Duong,<sup>†,ID</sup> Gihun Ryu,<sup>†</sup> Alexander Hoyer,<sup>†</sup> Chengtian Lin,<sup>†</sup> Marko Burghard,<sup>\*,†</sup> and Klaus Kern<sup>†,‡</sup>

<sup>†</sup>Max Planck Institute for Solid State Research, Heisenbergstrasse 1, D-70569 Stuttgart, Germany

<sup>‡</sup>Institut de Physique, École Polytechnique Fédérale de Lausanne, CH-1015 Lausanne, Switzerland

## S Supporting Information

**ABSTRACT:** Raman scattering is a powerful tool for investigating the vibrational properties of two-dimensional materials. Unlike the 2H phase of many transition metal dichalcogenides, the 1T phase of TiSe<sub>2</sub> features a Raman-active shearing and breathing mode, both of which shift toward lower energy with increasing number of layers. By systematically studying the Raman signal of 1T-TiSe<sub>2</sub> in dependence of the sheet thickness, we demonstrate that the charge density wave transition of this compound can be reliably determined from the temperature dependence of the peak position of the E<sub>g</sub> mode near 136 cm<sup>-1</sup>. The phase transition temperature is found to first increase with decreasing thickness of the sheets, followed by a decrease due to the effect of surface oxidation. The Raman spectroscopy-based method is expected to be applicable also to other 1T-phase transition metal dichalcogenides featuring a charge density wave transition and represents a valuable complement to electrical transport-based approaches.



**KEYWORDS:** 2D transition metal dichalcogenides, 1T-TiSe<sub>2</sub>, charge density wave transition, low-frequency Raman modes, shearing mode

The charge density wave (CDW), or distorted charge wave phase, has been extensively studied for many decades.<sup>1,2</sup> It comprises a structural transition from a normal to a distorted phase, driven by the competition between the energy gain due to the formation of an electronic energy gap, which redistributes the electronic levels to lower energies, and the energy cost associated with the distortion of the crystal structure.<sup>2</sup> The CDW transition occurs in many different types of materials, a prominent example being the metallic transition metal dichalcogenides (TMDCs) such as 2H-NbSe<sub>2</sub> or 1T-TiSe<sub>2</sub>, wherein the cohesive bonding between metal and chalcogenide is quite weak.<sup>3</sup> The nonlinear electrical characteristics of the CDW phase, which can be controlled by electrostatic gating, open up potential applications of CDW materials in electronic devices.<sup>2,4</sup> Furthermore, the competition of CDW and superconducting phases, leading to a dome shape like in case of high-T<sub>c</sub> superconductivity, is currently only little understood.<sup>5–8</sup>

Two-dimensional (2D) TMDCs are attracting great attention due to the dimensional dependence of their properties, including the CDW phase transition.<sup>9–15</sup> It has been shown that the transition temperature of the CDW phase of 2H-NbSe<sub>2</sub> increases upon decreasing the thickness of the exfoliated sheets.<sup>11</sup> In 1T-TaS<sub>2</sub>, by contrast, the transition from the incommensurate to the nearly commensurate CDW phase

is almost independent of the number of layers, while the transition from the nearly commensurate to the commensurate CDW phase is shifted toward lower temperature with decreasing sample thickness.<sup>14,15</sup> The detailed origin of this behavior has yet to be identified. Particularly interesting is the possibility to tune the CDW transition temperature of a thin TMDC sample through electrostatic gating or strain engineering.<sup>9,14,15</sup> This might enable controlling the quantum phase transition in a manner compatible with semiconductor technology.<sup>16,17</sup>

Bulk 1T-TiSe<sub>2</sub> undergoes a CDW transition from the 1 × 1 × 1 normal phase to the 2 × 2 × 2 CDW phase at 200 K.<sup>18</sup> While the underlying mechanism is still under debate, it has been suggested to involve Fermi surface nesting, the Jahn–Teller effect or a periodic lattice distortion (PLD), or excitons.<sup>17,19–21</sup> A recent study using ultrabroadband THz pulses points toward PLD as the main driving force for the formation of the CDW phase in TiSe<sub>2</sub>.<sup>20</sup> Similar conclusions have been drawn from density functional theory (DFT)-based simulations.<sup>17,19</sup> The existence of a superconductivity dome has

**Received:** November 16, 2016

**Accepted:** January 3, 2017

**Published:** January 3, 2017



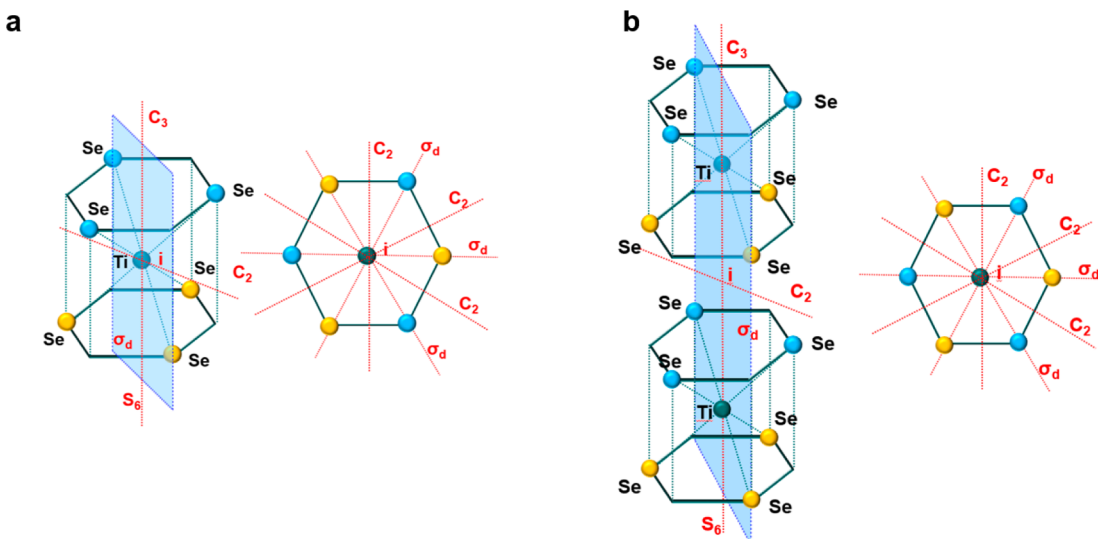


**Figure 1.** Symmetry analysis of a 1T-TiSe<sub>2</sub> (a) mono- and (b) bilayer. The space group  $D_{3d}^3$  with the corresponding  $C_3$ ,  $C_2$ ,  $\sigma_d$ ,  $S_6$ , and  $i$  symmetry operators, is preserved down to the thinnest sheets. The representation of the lattice modes depends on whether the thin sheets comprise an odd or even number of layers.

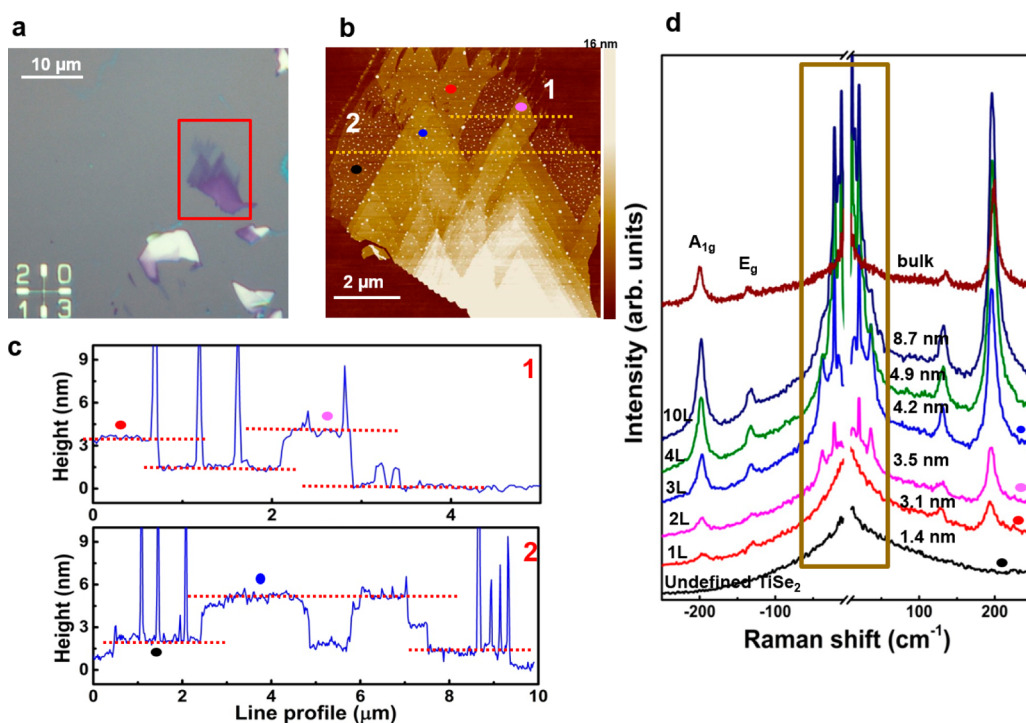


**Figure 2.** (a) Optical micrograph and (b) AFM image of exfoliated TiSe<sub>2</sub> sheets (corresponding to the region marked by the red rectangle in panel (a)). (c) Height profiles taken along the two dashed, horizontal lines in panel (b). (d) Room-temperature Raman spectra ( $\lambda = 633 \text{ nm}$ ) recorded from regions of different thickness of the sheet in panel (b). While the low-frequency shearing and breathing modes are absent in bulk TiSe<sub>2</sub>, they are clearly visible in the thin sheets.

been experimentally confirmed by subjecting bulk TiSe<sub>2</sub> to pressure or compositional doping.<sup>8,5</sup> Angle-resolved photo-emission spectroscopy (ARPES) has revealed the CDW transition in TiSe<sub>2</sub> monolayers on graphene, although different values of  $T_c$  have been obtained in these experiments.<sup>10,12</sup> Thus, the question of whether the CDW is enhanced or suppressed upon thinning the samples down to atomic thickness has not yet been resolved. Moreover, only very little has been reported on the possible use of the low-frequency Raman modes of the 1T-phase of TiSe<sub>2</sub> for determining the number of layers.<sup>22</sup>

Here, we experimentally and theoretically investigate the dependence of the low-frequency Raman modes and CDW transition of TiSe<sub>2</sub> on the number of layers. Our density functional perturbation theory (DFPT) simulations predict an enhancement of the CDW phase upon decreasing the thickness of the sheets. This trend is experimentally confirmed for sheet thicknesses down to 10 nm, reaching a value of 210 K, whereas for thinner sheets the substrate influence and oxidation under ambient conditions cause a reduction of  $T_c$ . In particular, we present a Raman spectroscopy-based approach to determine

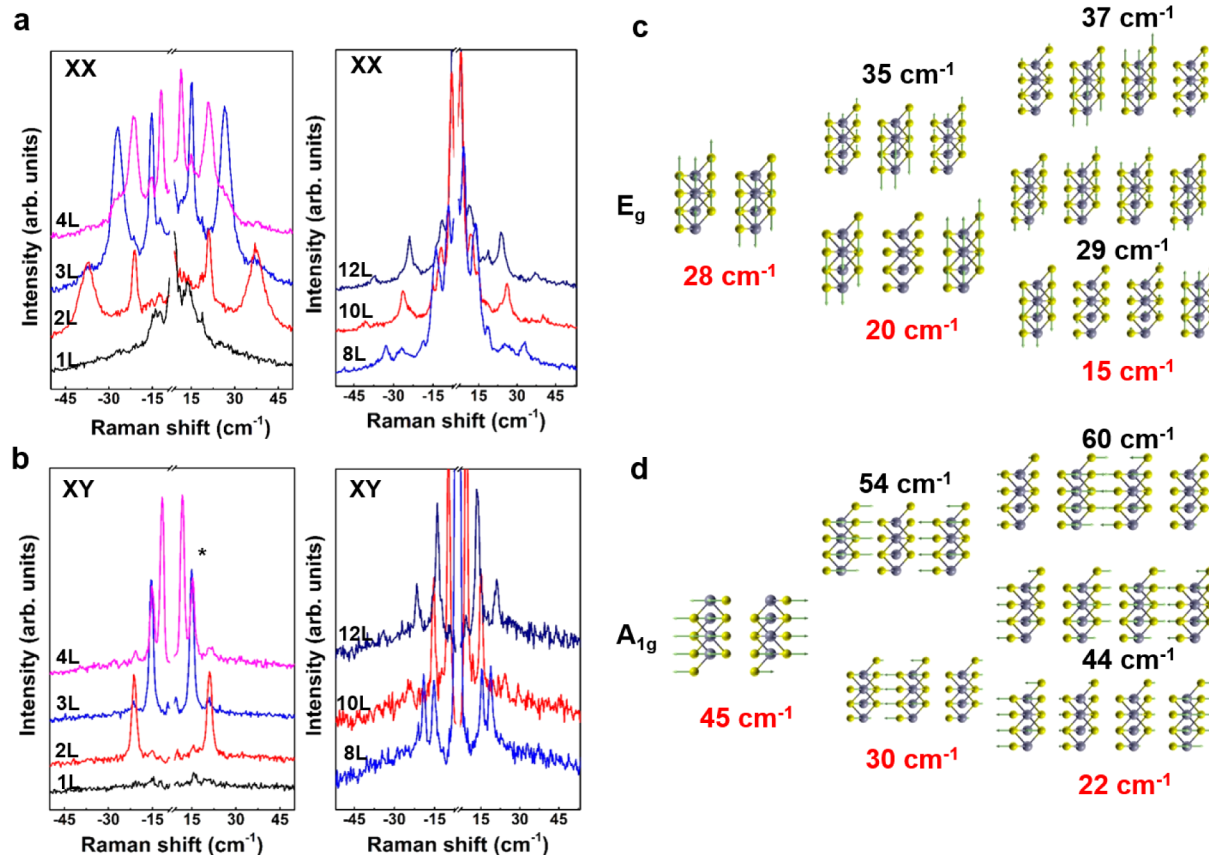


**Figure 3.** Room-temperature Raman spectra of thin TiSe<sub>2</sub> sheets, acquired with  $\lambda = 633$  nm in (a) XX and (b) XY polarization configuration. Atomic displacements associated with the (c) shearing and (d) breathing mode in TiSe<sub>2</sub> sheets of different thickness, as calculated by DFT-LDA. (\*) Raman signal contribution from the adjacent, three-layer-thick region.

the CDW transition temperature ( $T_c$ ) of 1T-TiSe<sub>2</sub>, which exploits the peak position of the E<sub>g</sub> mode (around 136 cm<sup>-1</sup>).

## RESULTS AND DISCUSSION

The crystal structure of 1T-TiSe<sub>2</sub> belongs to the symmorphic P3m1 ( $D_{3d}^3$ ) space group with one Ti and two Se atoms in the unit cell.<sup>18,23–25</sup> The corresponding factor group at the gamma point is isomorphic to the point group  $D_{3d}$  (see the irreducible representation in Table S1). The representation of the lattice vibration is decomposed as  $\Gamma_{\text{lat.mod.}} = A_{1g} + E_g + 2A_{2u} + 2E_{2u}$ . Unlike the 2H-phase of TMDCs (like 2H-MoS<sub>2</sub>), the crystal symmetry of bulk TiSe<sub>2</sub> is preserved for the thinnest sheets, as shown in Figure 1 for the mono- and bilayer.<sup>26–28</sup> However, the lattice mode representation depends on whether the number of TiSe<sub>2</sub> layers  $n$  is odd or even. For an odd number of layers, the Ti atom is located on three C<sub>2</sub> axes, whose crossing point represents a center of inversion, whereas for an even number there is no atom at this location. Accordingly, the number of equivalent atoms is different in the two cases (Table S1). The lattice vibrational modes in sheets with an odd and even number of layers are designated as  $\Gamma_{\text{lat.mod.}(odd)} = \frac{3n-1}{2}(A_{1g} + E_g) + \frac{3n+1}{2}(A_{2u} + E_u)$  and  $\Gamma_{\text{lat.mod.}(even)} = \frac{3n}{2}(A_{1g} + E_g + A_{2u} + E_u)$ , respectively. Among these, the modes belonging to A<sub>1g</sub> and E<sub>g</sub> are Raman active. Our symmetry analysis is in accordance with previous reports on 1T-PtS<sub>2</sub>, which has a similar lattice structure.<sup>22</sup>

Figure 2a shows an optical micrograph of mechanically exfoliated TiSe<sub>2</sub> sheets on a Si/SiO<sub>2</sub> substrate. Sheets of

different thickness can be readily distinguished by their contrast. The corresponding topographic AFM image (Figure 2b) and height profiles (Figure 2c) signify the layered structure of TiSe<sub>2</sub> with many step edges and an interlayer distance of approximately  $0.6 \pm 0.2$  nm. In Figure 2d, the Raman spectrum of bulk TiSe<sub>2</sub> is compared to spectra collected from sheet regions of different thickness. The two main Raman peaks in the bulk spectrum at 136 and 200 cm<sup>-1</sup> correspond to the E<sub>g</sub> and A<sub>1g</sub> mode, respectively. The Raman data in Figure 2d are consistent with previous reports.<sup>18,22–24</sup> The peaks at 233 and 316 cm<sup>-1</sup>, which can be attributed to defect-enabled phonons at the L and M points<sup>24</sup> according to previous theoretical work, are absent for the clean (freshly cleaved) surface at both high and low temperature in our measurements (Figure S1).<sup>29</sup> Moreover, the peak at 233 cm<sup>-1</sup> occurs after longer exposure to the ambient environment. Raman signals below 50 cm<sup>-1</sup> emerge for TiSe<sub>2</sub> sheets with a thickness of less than 10 nm. As the unit cell of bulk TiSe<sub>2</sub> consists of only one layer, no low-frequency modes corresponding to the shearing and breathing mode are observed in bulk TiSe<sub>2</sub>. However, these two (interlayer) modes appear for thin sheets, due to breaking of the translation symmetry along the z-axis. The actual number of TiSe<sub>2</sub> layers cannot be determined from AFM data alone. However, step edges can easily be identified in the AFM images (as exemplified by Figure 2d, where the height increase from 3.5 nm to 4.2 nm corresponds to a TiSe<sub>2</sub> monolayer). In order to identify a monolayer region, the Raman spectrum provides additional valuable information. Specifically, the thinnest areas displaying Raman features at 136 and 200 cm<sup>-1</sup> without peaks

in the low-frequency range can be assigned to a monolayer. For the sheet in **Figure 2b**, this is the case for the 3.1 nm thick region (see spectrum in **Figure 2d**). In principle, the intensity of the Raman peaks would be expected to gradually increase with increasing  $\text{TiSe}_2$  sheet thickness, as it is indeed observed for the two peaks at 136 and 200  $\text{cm}^{-1}$ , respectively. However, this is not the case for the peaks in the low-frequency range (below  $\sim 60 \text{ cm}^{-1}$ ), where pronounced peaks suddenly emerge starting from a sheet thickness of 3.5 nm. This observation supports the assignment of the 3.1 nm thick region to an effective monolayer that is surrounded by oxidized material. Another indication for oxidation under ambient conditions is the fact that the 1.4 nm thick region within the sheet of **Figure 2b** does not display any Raman signal (black line in **Figure 2d**). As shown in **Figure S2**, the low-frequency modes undergo a notable change upon increasing sample exposure to air. In fact, after keeping the sample for 3 h in air, the main peak at 12  $\text{cm}^{-1}$  has changed into two peaks located at 14 and 10  $\text{cm}^{-1}$ , respectively. Thus, the oxidation of thin  $\text{TiSe}_2$  sheets can be monitored using the low-energy peaks, whereas the Raman modes at 136 and 200  $\text{cm}^{-1}$  remain essentially unaffected by the air.

The shearing mode involves vibration in the  $xy$ -plane, while the breathing mode is associated with out-of-plane vibration along the perpendicular ( $z$ ) direction. Hence, the shearing (breathing) mode is 2-fold degenerate (nondegenerate) and belongs to the  $E_g$  ( $A_{1g}$ ) irreducible representation. This renders the Raman tensors of the two types of modes different (**Table S2**). While  $E_g$  modes can be detected in both XX and XY polarization configuration,  $A_{1g}$  modes appear only in the XX configuration.<sup>26–28</sup> Thus, the shearing and breathing mode can be distinguished with the aid of polarized Raman spectroscopy. **Figure 3a** and b show the Raman modes below 50  $\text{cm}^{-1}$ , acquired from various thin  $\text{TiSe}_2$  sheets in XX and XY configuration, respectively. In the case of the monolayer, no Raman peaks are observed in this range. By contrast, the sheets composed of two, three, or four layers display two well-defined peaks in the XX configuration, with one of them disappearing in the XY configuration. On the basis of the above symmetry analysis, we assign the peaks in **Figure 3b** to the shearing mode, while the additional peaks visible in XX configuration (**Figure 3a**) are attributed to the breathing mode. The shearing mode is shifted to lower energy with increasing number of layers, a trend that is opposite that of 2H-stacked layered materials, such as 2H- $\text{MoS}_2$ <sup>26,28,29</sup> but similar to the 1T-like structures such as  $\text{PtSe}_2$  and  $\text{Bi}_2\text{Se}_3$ .<sup>22,30</sup> This difference can be rationalized by a linear chain model.<sup>31</sup> The frequency  $\omega_i$  of the  $i$ th shearing vibration is given by  $\omega_i^2 = \frac{1}{2\pi^2 c^2 \mu} \left\{ 1 - \cos \left[ \frac{(i-1)\pi}{N} \right] \right\}$ , where  $c$  is the velocity of light,  $\alpha$  is the interlayer shearing force, and  $\mu$  is the mass per unit area of one layer. In the case of the 2H structure, the highest frequency branch ( $i = N$ ) vibration is detected.<sup>31</sup> In 1T- $\text{TiSe}_2$ , the lowest frequency branch is observed with  $i = 2$ . Therefore, the shearing mode frequency in the T-phase is  $\omega_2^2 = \frac{1}{2\pi^2 c^2 \mu} \left[ 1 - \cos \left( \frac{\pi}{N} \right) \right]$ . It follows that upon increasing the number of layers  $N$ , the shearing mode shifts to lower energy. We could gain further support for this trend from DFPT-based simulations of the shearing and breathing mode, as illustrated in **Figure 3c** and d, where the lowest energy modes (wavenumbers in red) belong to the measured Raman peaks.<sup>32,33</sup> The theoretical values slightly exceed the experimental ones, as the local density approximation overestimates the interlayer interaction. Sheets

composed of more than four layers display multiple Raman peaks, which can be assigned to higher frequency branches of the shearing and breathing modes. The low-frequency modes are useful to determine the number of layers within different regions of extended  $\text{TiSe}_2$  sheets from Raman maps (**Figure S3**). The interlayer shear and breathing force constants extracted using the linear chain model (**Figure S4**) are listed in **Table 1**.

**Table 1. Position of Shearing and Breathing Modes**

	bilayer	trilayer	quadruple layer	force constant ( $10^{19} \text{ N m}^{-3}$ )	
				exptl	DFT(LDA)
shearing mode ( $\text{cm}^{-1}$ )	21	15	12	2.2	3.8
breathing mode ( $\text{cm}^{-1}$ )	37	26	21	6.6	9.4

The normal phase of  $\text{TiSe}_2$  changes to the distorted phase below the transition temperature,  $T_c$ . The CDW phase transition can be monitored by changes in the Raman spectrum as well as in the electrical transport characteristics. **Figure 4a** shows the evolution of the Raman spectrum of bulk  $\text{TiSe}_2$  with temperature. Upon cooling, there appear two new peaks at 70 ( $E_g$ ) and 110 ( $A_{1g}$ )  $\text{cm}^{-1}$ , respectively, indicating the transition to the CDW phase.<sup>18,23,25</sup> These two peaks are associated with the transverse acoustic phonon mode at the L and M points, which folds to the gamma point in the  $2 \times 2 \times 2$  CDW reciprocal lattice.<sup>23,25</sup> Here, we term these two peaks “softened modes”. One option to determine the transition temperature relies upon the temperature dependence of the softened mode intensity (**Figure 4b**), analogous to the phase transition of  $\text{NbSe}_2$ .<sup>11</sup> In this manner, the transition temperature of bulk  $\text{TiSe}_2$  is estimated to be 180 K, somewhat lower than the  $T_c$  of 200 K derived from electrical transport measurements (**Figure S5**). This discrepancy arises from the weak temperature dependence of the softened modes in  $\text{TiSe}_2$ , due to which clear peaks are observable only at temperatures below  $T_c$ , and accordingly the peak intensities are difficult to determine. Although it is possible to minimize the error by increasing the spectral acquisition time and the laser power, this is time intensive and involves the risk of sample heating. These problems can be avoided by evaluating the  $E_g$  Raman peak at 136  $\text{cm}^{-1}$ , relating to the in-plane vibration of two Se atoms around the Ti atom. This vibrational mode exists in both the normal and the CDW phase of 1T- $\text{TiSe}_2$ . As apparent from **Figure 4c**, upon cooling, this mode initially shifts to higher energy. Such behavior is expected due to phonon hardening with decreasing temperature. However, upon further cooling below 195 K, the peak position reverses back to that at room temperature. Importantly, the transition temperature of 195 K coincides with  $T_c$  of the CDW phase, establishing a reliable and straightforward means to experimentally determine  $T_c$ . This method is much easier and more accurate than tracing the softened mode intensities. By contrast, the  $A_{1g}$  peak near 200  $\text{cm}^{-1}$  is not suitable for this purpose, as it monotonically increases upon cooling (**Figure S6**). In fact, the  $A_{1g}$  mode is associated with the out-of-plane vibration of Se atoms around a Ti atom and is therefore insensitive to the CDW phase transition accompanied by a strong in-plane distortion. It is noteworthy that the corresponding peak in 1T- $\text{TaS}_2$  displays a

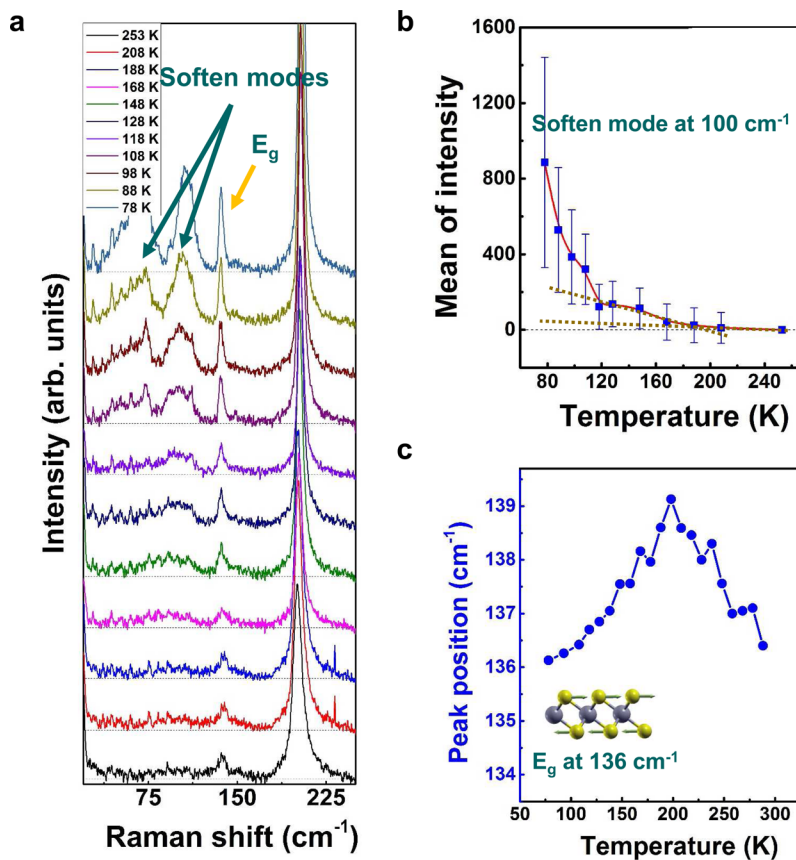


**Figure 4.** (a) Evolution of the Raman spectrum ( $\lambda = 633$  nm) of bulk TiSe<sub>2</sub> with temperature. (b) Averaged intensity of the softened mode at  $100\text{ cm}^{-1}$  as a function of temperature. The mean intensity corresponds to the average within the range of  $60$  to  $110\text{ cm}^{-1}$ . (c) Peak position of the E<sub>g</sub> mode near  $136\text{ cm}^{-1}$  in dependence of temperature.

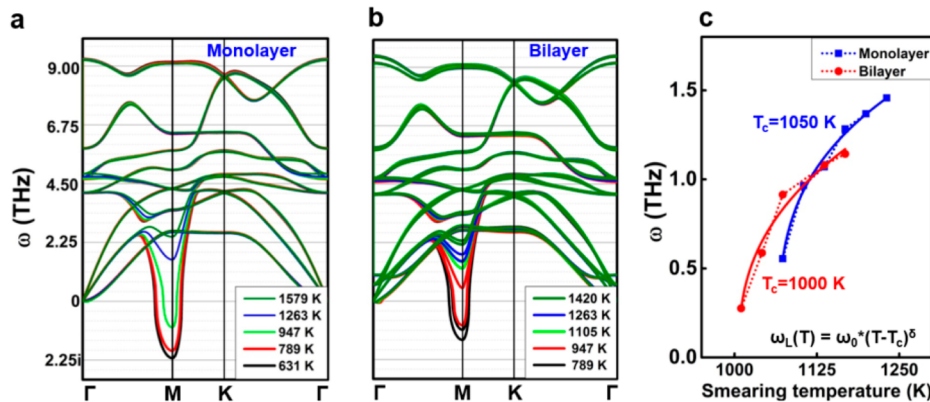


**Figure 5.** (a, b) Evolution of the phonon spectrum of monolayer (a) and bilayer (b) TiSe<sub>2</sub> with electronic temperature. (c) Fits of the electronic (smearing) temperature dependence of the frequency of the softened phonon mode at the M point, together with the extracted  $T_c$  values.

sharp, temperature-dependent change due to the first-order transition behavior of this compound.<sup>34</sup>

Of particular interest is the dependence of the CDW transition on the sheet thickness. In the case of 2H-NbSe<sub>2</sub> the  $T_c$  is higher for thin sheets as compared to the bulk material, whereas an opposite trend is observed for 1T-TaS<sub>2</sub>.<sup>11,14,15</sup> Toward predicting the thickness dependence of  $T_c$  for TiSe<sub>2</sub>, it is relevant that the CDW phase transition is driven by the redistribution of the electronic states, and accordingly a rough estimate can be made by investigating the change of the phonon spectrum with the electronic temperature.<sup>19</sup> To this

end, Figure 5a,b display the evolution of the phonon spectrum of monolayer and bilayer TiSe<sub>2</sub> with electronic temperature. The phonon softening observed at the M point is associated with the  $2 \times 2 \times 1$  CDW phase structure. Fitting the dependence with the equation  $\omega_L = \omega_0^*(T - T_c)^\delta$  yields a  $T_c$  of 1000 and 1050 K for the bilayer and monolayer TiSe<sub>2</sub>, respectively, as shown in Figure 5c. Comparison with the bulk value on the order of 600 K, as predicted by theory, signifies that  $T_c$  increases upon decreasing the TiSe<sub>2</sub> sample thickness.<sup>19</sup>

In order to determine the dependence of  $T_c$  on the thickness of TiSe<sub>2</sub> sheets experimentally, we evaluate the E<sub>g</sub> peak position

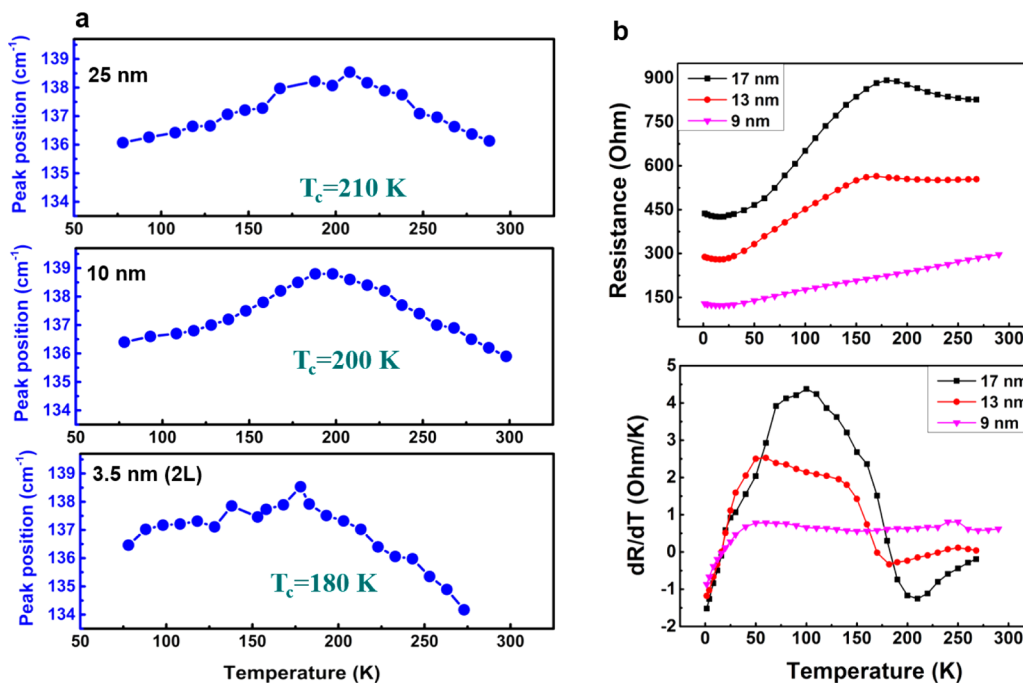


**Figure 6.** (a) Peak position of the  $E_g$  mode near  $136 \text{ cm}^{-1}$  as a function of temperature for three TiSe<sub>2</sub> sheets of different thickness (2L denotes a bilayer). (b) Temperature dependence of electrical resistance (top plot) and the temperature derivative of resistance (bottom plot) for three TiSe<sub>2</sub> sheets of different thickness.

as a function of temperature for sheets with a thickness of 25 nm, 10 nm, and bilayer TiSe<sub>2</sub>, respectively (see Figure 6a).<sup>35</sup> For the 25 nm thick sheet,  $T_c$  is 210 K, notably above the bulk value of 195 K. This increase can be attributed to enhanced electron–phonon interaction, in close correspondence to the behavior of 2H-NbSe<sub>2</sub> and our theoretical simulation.<sup>11</sup> However,  $T_c$  decreases upon further decreasing the sheet thickness, reaching 200 K for a thickness of 10 nm and 180 K for bilayer TiSe<sub>2</sub>. The same trend is apparent from the resistance *vs* temperature plots in Figure 6b. It is most likely due to surface oxidation, similar to the effect of defects within bulk TiSe<sub>2</sub>, which have been documented to reduce the  $T_c$  of this compound.<sup>18</sup> As the highest  $T_c$  thus far reported for monolayer TiSe<sub>2</sub> is 230 K, observed on a monolayer grown on a graphene substrate by molecular epitaxy,<sup>10,12</sup> additional influence may arise from the substrate or intrinsic defects that are already present in the bulk<sup>18</sup> but whose density is further enhanced in the thin TiSe<sub>2</sub> sheets.

## CONCLUSIONS

In summary, we have studied the temperature-dependent Raman modes of 1T-TiSe<sub>2</sub> down to monolayer thickness. The low-frequency shearing and breathing modes, which do not exist in the bulk form, are shown to be suitable for determining the number of layers in thin TiSe<sub>2</sub> sheets. In addition, we demonstrate a straightforward method to monitor the CDW transition in 1T-TiSe<sub>2</sub> *via* the temperature-dependent position of the  $E_g$  peak around  $136 \text{ cm}^{-1}$ . Thus derived transition temperatures agree well with values gained from electrical transport measurements. Major factors that limit the accuracy of the method are surface oxidation effects, the substrate influence, and intrinsic defects. Our findings suggest that the low-energy Raman modes in ultrathin 2D transition metal dichalcogenide layers could prove useful as more general probes such as for magnetic or electron–hole interactions.

## METHODS

Bulk TiSe<sub>2</sub> crystals were exfoliated by the Scotch tape method onto Si substrates covered by 300 nm of thermal SiO<sub>2</sub>. Standard e-beam lithography and subsequent metal evaporation were used to define Ti/Au (2/40 nm) electrodes on top of the exfoliated sheets. Raman spectroscopy was performed in air (unless otherwise noted) with a laser wavelength of 633 nm combined with an 1800 g/mm grating, with a resolution of  $0.34 \text{ cm}^{-1}$ . In order to access the Stokes and anti-Stokes Raman modes at low frequency, a Bragg filter was used ( $\pm 10 \text{ cm}^{-1}$  cutoff around the laser line). The laser power was kept below 0.1 mW to minimize sample heating. The samples were cooled inside a Linkam THMS600 cryostat using liquid N<sub>2</sub>. Electrical transport measurements were carried out in four-probe configuration down to 1.5 K in a liquid helium cryostat. The energy of the vibrational modes was calculated by the Quantum Espresso code.<sup>36</sup> The exchange–correlation interaction was calculated by the local density approximation.<sup>37</sup> The  $24 \times 24 \times 12$  k-point grid with the projector augmented wave (PAW) potential was implemented by a cutoff energy of 80 Ry for all calculations.<sup>38</sup> The phonon dispersion was calculated as previously reported.<sup>19</sup> The transition temperature was determined from the maximum peak position of the  $E_g$  mode around  $136 \text{ cm}^{-1}$ . As the temperature difference between two measurements is 10 K, the error of  $T_c$  is  $\pm 5 \text{ K}$ .

## ASSOCIATED CONTENT

### S Supporting Information

The Supporting Information is available free of charge on the ACS Publications website at DOI: [10.1021/acsnano.6b07737](https://doi.org/10.1021/acsnano.6b07737).

Supporting Information detailing supplementary text and Figures S1 to S7 (PDF)

## AUTHOR INFORMATION

### Corresponding Author

\*Tel: +49-(0711) 689-1448. Fax: +49-(0711) 689-1662. E-mail: [m.burghard@fkf.mpg.de](mailto:m.burghard@fkf.mpg.de).

## ORCID

Dinh Loc Duong: 0000-0002-4118-9589

## Notes

The authors declare no competing financial interest.

## ACKNOWLEDGMENTS

The DFPT calculations were performed in Karlsruhe Institute of Technology (KIT) within the ELCPHON project.

## REFERENCES

- (1) Grüner, G. The Dynamics of Charge-Density Waves. *Rev. Mod. Phys.* **1988**, *60*, 1129–1181.
- (2) Thorne, R. E. Charge-Density-Wave Conductors. *Phys. Today* **1996**, *49*, 42–47.
- (3) Crystallography and Crystal Chemistry of Materials with Layered Structures; Levy, F., Ed.; Springer, 1976.
- (4) Adelman, T. L.; Zaitsev-Zotov, S. V.; Thorne, R. E. Field-Effect Modulation of Charge-Density-Wave Transport in NbSe<sub>3</sub> and TaS<sub>3</sub>. *Phys. Rev. Lett.* **1995**, *74*, 5264–5267.
- (5) Morosan, E.; Zandbergen, H. W.; Dennis, B. S.; Bos, J. W. G.; Onose, Y.; Klimczuk, T.; Ramirez, A. P.; Ong, N. P.; Cava, R. J. Superconductivity in Cu<sub>x</sub>TiSe<sub>2</sub>. *Nat. Phys.* **2006**, *2*, 544–550.
- (6) Qi, Y.; Naumov, P. G.; Ali, M. N.; Rajamathi, C. R.; Barkalov, O.; Hanfland, M.; Wu, S.-C.; Shekhar, C.; Sun, Y.; Süß, V.; Schmidt, M.; Schwarz, U.; Pippel, E.; Werner, P.; Hillebrand, R.; Förster, T.; Kampert, E.; Parkin, S.; Cava, R. J.; Felser, C.; et al. Superconductivity in Weyl Semimetal Candidate MoTe<sub>2</sub>. *Nat. Commun.* **2015**, *95*, 2–5.
- (7) Calandra, M.; Mauri, F. Charge-Density Wave and Superconducting Dome in TiSe<sub>2</sub> from Electron-Phonon Interaction. *Phys. Rev. Lett.* **2011**, *106*, 196406.
- (8) Kusmartseva, A. F.; Sipos, B.; Berger, H.; Forró, L.; Tuttiš, E. Pressure Induced Superconductivity in Pristine TiSe<sub>2</sub>. *Phys. Rev. Lett.* **2009**, *103*, 236401.
- (9) Li, L. J.; O'Farrell, E. C. T.; Loh, K. P.; Eda, G.; Özyilmaz, B.; Castro Neto, A. H. Controlling Many-Body States by the Electric-Field Effect in a Two-Dimensional Material. *Nature* **2015**, *529*, 185–189.
- (10) Sugawara, K.; Nakata, Y.; Shimizu, R.; Han, P.; Hitosugi, T.; Sato, T.; Takahashi, T. Unconventional Charge-Density-Wave Transition in Monolayer 1T-TiSe<sub>2</sub>. *ACS Nano* **2016**, *10*, 1341–1345.
- (11) Xi, X.; Zhao, L.; Wang, Z.; Berger, H.; Forró, L.; Shan, J.; Mak, K. F. Strongly Enhanced Charge-Density-Wave Order in Monolayer NbSe<sub>2</sub>. *Nat. Nanotechnol.* **2015**, *10*, 1–6.
- (12) Chen, P.; Chan, Y.-H.; Fang, X.-Y.; Zhang, Y.; Chou, M. Y.; Mo, S.-K.; Hussain, Z.; Fedorov, A.-V.; Chiang, T.-C. Charge Density Wave Transition in Single-Layer Titanium Diselenide. *Nat. Commun.* **2015**, *6*, 8943.
- (13) Mak, K. F.; Lee, C.; Hone, J.; Shan, J.; Heinz, T. F. Atomically Thin MoS<sub>2</sub>: A New Direct-Gap Semiconductor. *Phys. Rev. Lett.* **2010**, *105*, 136805.
- (14) Yu, Y.; Yang, F.; Lu, X. F.; Yan, Y. J.; Cho, Y.; Ma, L.; Niu, X.; Kim, S.; Son, Y.; Feng, D.; Li, S.; Cheong, S.-W.; Chen, X. H.; Zhang, Y. Gate-Tunable Phase Transitions in Thin Flakes of 1T-TaS<sub>2</sub>. *Nat. Nanotechnol.* **2015**, *10*, 270–276.
- (15) Yoshida, M.; Zhang, Y.; Ye, J.; Suzuki, R.; Imai, Y.; Kimura, S.; Fujiwara, A.; Iwasa, Y. Controlling Charge-Density-Wave States in Nano-Thick Crystals of 1T-TaS<sub>2</sub>. *Sci. Rep.* **2014**, *4*, 7302.
- (16) Abbamonte, P. 2D Superconductivity: Electric Tuning of Many-Body States. *Nat. Nanotechnol.* **2016**, *11*, 115–116.
- (17) Calandra, M. 2D Materials: Charge Density Waves Go Nano. *Nat. Nanotechnol.* **2015**, *10*, 737–738.
- (18) Di Salvo, F. J.; Moncton, D. E.; Waszczak, J. V. Electronic Properties and Superlattice Formation in the Semimetal TiSe<sub>2</sub>. *Phys. Rev. B* **1976**, *14*, 4321–4328.
- (19) Duong, D. L.; Burghard, M.; Schön, J. C. *Ab Initio* Computation of the Transition Temperature of the Charge Density Wave Transition in TiSe<sub>2</sub>. *Phys. Rev. B: Condens. Matter Mater. Phys.* **2015**, *92*, 245131.
- (20) Porer, M.; Leierseder, U.; Ménard, J.-M.; Dachraoui, H.; Mouchliadis, L.; Perakis, I. E.; Heinemann, U.; Demsar, J.; Rossnagel, K.; Huber, R. Non-Thermal Separation of Electronic and Structural Orders in a Persisting Charge Density Wave. *Nat. Mater.* **2014**, *13*, 1–19.
- (21) Monney, C.; Battaglia, C.; Cercellier, H.; Aebi, P.; Beck, H. Exciton Condensation Driving the Periodic Lattice Distortion of 1T-TiSe<sub>2</sub>. *Phys. Rev. Lett.* **2011**, *106*, 1–4.
- (22) Zhao, Y.; Qiao, J.; Yu, P.; Hu, Z.; Lin, Z.; Lau, S. P.; Liu, Z.; Ji, W.; Chai, Y. Extraordinarily Strong Interlayer Interaction in 2D Layered PtS<sub>2</sub>. *Adv. Mater.* **2016**, *28*, 2399–2407.
- (23) Holy, J. A.; Woo, K. C.; Klein, M. V.; Brown, F. C. Raman and Infrared Studies of Superlattice Formation in TiSe<sub>2</sub>. *Phys. Rev. B* **1977**, *16*, 3628–3637.
- (24) Uchida, S.; Sugai, S. Infrared and Raman Studies on Commensurate CDW States in Transition Metal Dichalcogenides. *Physica B+C* **1981**, *105*, 393–399.
- (25) Jaswal, S. S. Lattice Dynamics of TiSe<sub>2</sub>. *Phys. Rev. B: Condens. Matter Mater. Phys.* **1979**, *20*, 5297.
- (26) Zhang, X.; Han, W. P.; Wu, J. B.; Milana, S.; Lu, Y.; Li, Q. Q.; Ferrari, A. C.; Tan, P. H. Raman Spectroscopy of Shear and Layer Breathing Modes in Multilayer MoS<sub>2</sub>. *Phys. Rev. B: Condens. Matter Mater. Phys.* **2013**, *87*, 1–8.
- (27) Zhang, X.; Tan, Q.-H.; Wu, J.-B.; Shi, W.; Tan, P.-H. Review on the Raman Spectroscopy of Different Types of Layered Materials. *Nanoscale* **2016**, *8*, 6435–6450.
- (28) Zhao, Y.; Luo, X.; Li, H.; Zhang, J.; Araujo, P. T.; Gan, C. K.; Wu, J.; Zhang, H.; Quek, S. Y.; Dresselhaus, M. S.; Xiong, Q. Interlayer Breathing and Shear Modes in Few-Trilayer MoS<sub>2</sub> and WSe<sub>2</sub>. *Nano Lett.* **2013**, *13*, 1007–1015.
- (29) Lorchat, E.; Froehlicher, G.; Berciaud, S. Splitting of Interlayer Shear Modes and Photon Energy Dependent Anisotropic Raman Response in N-Layer ReSe<sub>2</sub> and ReS<sub>2</sub>. *ACS Nano* **2016**, *10*, 2752–2760.
- (30) Zhao, Y.; Luo, X.; Zhang, J.; Wu, J.; Bai, X.; Wang, M.; Jia, J.; Peng, H.; Liu, Z.; Quek, S. Y.; Xiong, Q. Interlayer Vibrational Modes in Few-Quintuple-Layer Bi<sub>2</sub>Te<sub>3</sub> and Bi<sub>2</sub>Se<sub>3</sub> Two-Dimensional Crystals: Raman Spectroscopy and First-Principles Studies. *Phys. Rev. B: Condens. Matter Mater. Phys.* **2014**, *90*, 1–11.
- (31) Tan, P.; Han, W.; Zhao, W.; Wu, Z. The Shear Mode of Multilayer Graphene. *Nat. Mater.* **2012**, *11*, 294–300.
- (32) Luo, X.; Zhao, Y.; Zhang, J.; Toh, M.; Kloc, C.; Xiong, Q.; Quek, S. Y. Effects of Lower Symmetry and Dimensionality on Raman Spectra in Two-Dimensional WSe<sub>2</sub>. *Phys. Rev. B: Condens. Matter Mater. Phys.* **2013**, *88*, 1–7.
- (33) Luo, X.; Zhao, Y.; Zhang, J.; Xiong, Q.; Quek, S. Y. Anomalous Frequency Trends in MoS<sub>2</sub> Thin Films Attributed to Surface Effects. *Phys. Rev. B: Condens. Matter Mater. Phys.* **2013**, *88*, 1–13.
- (34) He, R.; Okamoto, J.; Ye, Z.; Ye, G.; Anderson, H.; Dai, X.; Wu, X.; Hu, J.; Liu, Y.; Lu, W.; Sun, Y.; Pasupathy, A. N.; Tsien, A. W. Distinct Surface and Bulk Charge Density Waves in Ultrathin 1T-TaS<sub>2</sub>. *Phys. Rev. B: Condens. Matter Mater. Phys.* **2016**, *94*, 201108.
- (35) Goli, P.; Khan, J.; Wickramaratne, D.; Lake, R. K.; Balandin, A. a. Charge Density Waves in Exfoliated Films of van Der Waals Materials: Evolution of Raman Spectrum in TiSe<sub>2</sub>. *Nano Lett.* **2012**, *12*, 5941–5945.
- (36) Giannozzi, P.; Baroni, S.; Bonini, N.; Calandra, M.; Car, R.; Cavazzoni, C.; Ceresoli, D.; Chiarotti, G. L.; Cococcioni, M.; Dabo, I.; Corso, A. D.; Gironcoli, S.; Fabris, S.; Fratesi, G.; Gebauer, R.; Uwe, G.; Gougaussis, C.; Kokalj, A.; Lazzeri, M.; Martin-Samos, L.; et al. QUANTUM ESPRESSO: A Modular and Open-Source Software Project for Quantum Simulations of Materials. *J. Phys.: Condens. Matter* **2009**, *21*, 395502.
- (37) Perdew, J. P.; Zunger, A. Self-Interaction Correction to Density-Functional Approximations for Many-Electron Systems. *Phys. Rev. B: Condens. Matter Mater. Phys.* **1981**, *23*, 5048–5079.
- (38) Kucukbenli, E.; Monni, M.; Adetunji, B. I.; Ge, X.; Adebayo, G. A.; Marzari, N.; De Gironcoli, S.; Corso, A. D. Projector Augmented-Wave and All-Electron Calculations across the Periodic Table: A Comparison of Structural and Energetic Properties. (2014) <http://arxiv.org/abs/1404.3015> (Accessed Dec 12, 2016).